Available online at www.sciencedirect.com
ScienceDirect
Acta Materialia 58 (2010) 4199–4206
Acta MATERIALIA
www.elsevier.com/locate/actamat

Phase separation mediated devitrification of $Al_{88}Y_7Fe_5$ glasses

K.K. Sahu [a,b], N.A. Mauro [a,b], L. Longstreth-Spoor [a,b], D. Saha [a], Z. Nussinov [a,b], M.K. Miller [c], K.F. Kelton [a,b,*]

[a] Department of Physics, Washington University, St. Louis, MO 63130-4899, USA
[b] Center for Materials Innovation, Washington University, St. Louis, MO 63130-4899, USA
[c] Materials Science and Technology Division, Oak Ridge National Laboratory, Oak Ridge, TN 37831-613, USA

Received 23 October 2009; received in revised form 2 April 2010; accepted 7 April 2010
Available online 11 May 2010

Abstract

The mechanisms responsible for the nanoscale devitrification of Al-based metallic glasses are unclear. A particularly well-studied case is $Al_{88}Y_7Fe_5$, where non-isothermal differential scanning calorimetry (DSC) measurements show an exothermic peak that is consistent with glass devitrification to α-Al, but with no glass transition. Additionally, isothermal DSC studies show a monotonic decrease in enthalpy release with annealing, a feature generally taken to indicate grain coarsening. The results of coordinated DSC, bright field transmission electron microscopy, in situ electrical resistivity and atom probe tomography (APT) studies of $Al_{88}Y_7Fe_5$ support a nucleation/growth-based crystallization process. The APT data indicate the presence of sub-nanometer pure Al zones and coarser scale (separation distance ~74–126 nm) Al-rich regions in the glass. The pure Al zones dispersed in the Al-rich regions appear to catalyze α-Al nucleation, explaining the high nucleation rates. The solute-rich regions between the Al-rich regions inhibit long-range diffusion, explaining the low growth rates.

Keywords: Coarsening; Aluminum alloys; Phase separation; Nucleation and growth; Metallic glass

1. Introduction

Lightweight Al–rare-earth–transition metal (Al–RE–TM) metallic glasses typically have good corrosion resistance, high yield strength and other key properties that make them interesting for potential structural applications. However, in contrast with the discovery of bulk metallic glasses in several alloy families [1–3], essentially all of the Al–RE–TM glasses require quenching rates of 10^5–10^6 °C s^{-1} for their formation, limiting their technological usefulness. Further, while appearing to be amorphous from X-ray diffraction and transmission electron microscopy (TEM) studies, many of these glasses show no discernible glass transition. The devitrification pathway is highly varied and extremely sensitive to small changes in composition [4,5]. Many of these glasses crystallize to nano-composite materials with an extremely high grain density (10^{21}–10^{23} m^3). The mechanisms for such a high nucleation rate, presumably the reason for poor bulk glass formability and the lack of a glass transition in the $Al_{88}Y_7Fe_5$ system, are not completely understood.

The devitrification of Al-based glasses has been studied extensively [6–11] and several explanations for the high nucleation rates have been presented. The growth of quenched-in nuclei has frequently been proposed [12–16]. However, during a rapid quench, the slowing in kinetics governing the evolution of the cluster distribution with decreasing temperature will cause the cluster population to deviate from that expected for steady-state nucleation [17]. As a result, the nucleation rate during the quench can be orders of magnitude lower than the steady-state rate [18]. Were the crystal density observed after annealing (of order 10^{21}–10^{23} m^{-3}) to arise from nuclei produced during

* Corresponding author at: Department of Physics, Washington University, St. Louis, MO 63130-4899, USA. Tel.: +1 314 935 6228; fax: +1 314 935 6219.
E-mail address: kfk@wustl.edu (K.F. Kelton).

1359-6454/$36.00 © 2010 Acta Materialia Inc. Published by Elsevier Ltd. All rights reserved.
doi:10.1016/j.actamat.2010.04.011

the quench, then the steady-state nucleation rates would appear to be unreasonably high.

Recently, three-dimensional atom probe tomography (APT) studies of $Al_{87}Ni_6La_5$ glasses showed chemical phase separation into regions of approximately 95% Al concentration [19]. The similarity between the number density of these regions ($\sim 5 \times 10^{23}$ m^{-3}) and the grain density of α-Al in the devitrified glass suggests that these regions are favorable sites for nucleation. There have been earlier reports of phase separation in metallic glasses [20–23]. However, these have often been based on observations of contrast fluctuations in TEM which can be artifacts from the TEM specimen preparation [24,25]. These artifacts are limited to sample surfaces [26] and no links have been established between these and chemical phase separation in interior of samples. While phase separation could explain the high nucleation rate in $Al_{88}Y_7Fe_5$, there have been no previous studies showing this.

Here, results from APT, differential scanning calorimetry (DSC), electrical resistivity, and TEM studies of the devitrification process in rapidly quenched $Al_{88}Y_7Fe_5$ alloys are presented. Previous studies by this group showed an isothermal DSC signature consistent with coarsening, suggesting that the rapidly quenched alloys were not glasses. However, the results presented here show that this is not the case. The anomalous DSC curves arise from an extremely high nucleation rate coupled with diffusion-limited growth. Further, our APT studies provide the first evidence for phase separation into regions of high Al concentration (with a spatial separation of approximately 74–126 nm) prior to crystallization in the quenched $Al_{88}Y_7Fe_5$ alloys. As in the $Al_{87}Ni_6La_5$ glasses, these regions appear to act as preferential sites for the nucleation of α-Al.

2. Experimental procedure

$Al_{88}Y_7Fe_5$ ingots were prepared by arc-melting mixtures of Al (99.99%, Alfa Aesar), Y (99.9%, Alfa Aesar), and Fe (99.98%, Alfa Aesar) on a water-cooled copper hearth in a chamber that had first been evacuated to ~4 Pa and backfilled with high-purity Ar gas (99.998%). A Ti/Zr getter located close to the sample was melted prior to arc-melting to further reduce the oxygen from the chamber. Each ingot was melted two to three times to ensure a homogeneous composition; the duration of each melt cycle was approximately 1 min. The ingots were melted by RF-induction heating to 1100–1150 °C (above the liquidus temperature) in a graphite crucible under an Ar atmosphere and rapidly quenched onto a copper wheel rotating at ~70 m s^{-1}, producing ribbons that were continuous for 3–10 cm, with an average cross-section of 1–2 mm by 20–30 μm.

The as-quenched ribbons were characterized by X-ray diffraction (Rigaku, Cu Kα, $\lambda = 1.54$ Å radiation), DSC (Perkin–Elmer, model DSC 7), and electrical resistivity measurements. In situ resistivity measurements were made using a four-probe technique, with a Fluke 8505A digital voltmeter and a computer-controlled switching circuit to reduce thermocouple effects [27]. For these studies, ribbons of ~3 cm length (~40 mg) were placed in an insulating MACOR® holder that was inserted into a furnace constructed from a large copper cylinder (~1 kg). The samples were initially held in a water-cooled copper block; they were inserted into the furnace after it had stabilized at the desired temperature. All measurements were made in Ti-gettered high-purity (99.995%) argon atmosphere. A thermocouple was used to monitor sample temperature; the thermal stability was typically ±0.1% over 80 h.

The sample microstructures of the as-quenched and annealed samples were examined using a JEOL 2000FX transmission electron microscope. TEM specimens were prepared by ion milling with liquid nitrogen cooling (GATAN, model 600). For the studies of annealed glasses, the ribbons were wrapped in aluminum foil and completely immersed in a lead–tin solder bath. The high thermal conductivity of the foil allowed the samples to reach the annealing temperature quickly; the large thermal mass of the bath enabled the temperature to remain stable over the duration of the anneal. High-resolution TEM (HRTEM) studies were made with a JEOL 2100F, using samples that were thinned by electropolishing in a mixture of nitric acid and methanol at 18 V DC.

Atom probe tomography measurements were made on as-quenched ribbons using the Imago Scientific Instruments Local Electrode Atom Probe (LEAP). The LEAP has a single atom crossed delay line detector and a 200 kHz voltage pulse generator. It has a maximum field of view of ~100 nm. Data sets of over 10^8 atoms can be obtained routinely. Two methods were used to prepare the sample tips for the APT measurements. In one case, a focused-ion-beam-based annular milling technique [28] was used to fabricate samples with 75–150 nm tip diameters. These samples showed a high failure rate in the LEAP so most samples were prepared by electropolishing in a solution of nitric acid and methanol at 12 V DC. The ribbons were first cut into 7–10 mm long sections and ground to an approximately square cross-section with 1000 grit sandpaper. A loop-based pulse polishing technique was used to polish these blanks into atom probe specimens [29]. Once prepared, the samples were quickly loaded into the LEAP to minimize oxidation. The chemical distribution of collected atoms was analyzed and confirmed to only deviate from the nominal composition by 0.01% for each species.

3. Results and discussion

3.1. DSC/coarsening calculation

Extensive DSC and X-ray diffraction (XRD) characterization studies of as-quenched $Al_{88}Y_7Fe_5$ have previously been reported [4,8,30]. The XRD patterns show the broad diffraction peaks characteristic of a glass, and

non-isothermal DSC scans show a peak corresponding to crystallization. Additionally, HRTEM studies produced no evidence of crystallites on any length scale in the as-quenched ribbons. However, there is no evidence of a glass transition in the non-isothermal scan. Also, the isothermal DSC data do not show the expected peak for a nucleation/growth-based transformation, but instead show an exothermic curve that decreases monotonically in magnitude with annealing time. This character of the isothermal DSC data has traditionally been associated with coarsening [31], but can also be explained by an extremely high nucleation rate with slow, diffusion-limited growth [32]. As was pointed out in an earlier publication [14], care must be taken when interpreting heating data for Al-based alloys since the crystal nucleation rates are so high that DSC studies of the transformation can be misleading.

As-quenched ribbons of $Al_{88}Y_7Fe_5$ were annealed at 250 °C ($T_x = 269$ °C) in a lead–tin bath to study microstructural development during crystallization. TEM bright field images of the as-cast ribbons were featureless, and the corresponding diffraction patterns showed broad rings, both consistent with amorphous samples. Spheroidal crystals are observed in the annealed ribbons, particularly for short annealing times, in contrast with the strongly dendritic grains commonly observed for many related aluminum alloy glasses [4,5,33].

The particle number density of crystallites increases with annealing times, which would seem to be inconsistent with coarsening, where the number density would be expected to decrease with time [34,35]. Due to poor contrast, arising from the TEM specimen thickness (50–100 nm) and medium-range order in the glass, it is difficult to definitively observe crystallites that are smaller than approximately 5 nm in diameter. It is possible, then, that such crystallites might be present in the as-cast samples. Additionally, if precipitation had gone to near completion, the size distribution of those precipitates would result in coarsening with annealing. Particles would grow to a visible size and thus appear to increase in number, mimicking nucleation. To examine this in more detail, the particle-size distribution was determined from TEM images of the as-quenched ribbon and after annealing times of 5, 10, 15, 20, 25, and 30 min. To accumulate adequate statistics, many images from different parts of the samples were taken to give a total of several hundred particles for the short annealing times and more than a thousand particles for longer annealing times. A spherical growth morphology was assumed for the analysis. While the number of crystallites observed is readily measured, it was necessary to use a probabilistic approach to reconstruct the three-dimensional particle-size distribution from the two dimensional projection measured by TEM. The commonly used approach of Saltykov [36] was followed. This method, which bins the observed particles into size classes, frequently generates negative values for smaller size classes, which are clearly not physical. However, a comparison with the distribution computed from another commonly used approach, the 25F association method [37], showed that the average radius was robust, with the values obtained from the two approaches agreeing to within 1% for all annealing times. The number of crystallites increases approximately linearly with annealing time at 250 °C, with a rate of $\sim 2 \times 10^{20}\,m^{-3}\,min^{-1}$ ($3 \times 10^{18}\,m^{-3}\,s^{-1}$), until saturation occurs at 20 min (Fig. 1).

In coarsening, larger crystallites grow at the expense of smaller ones due to the size-dependent chemical potential, which shifts the equilibrium concentration of solute at the interface according to the Gibbs–Thompson equation [38]. The Lifshitz, Slyozov and Wagner (LSW) [34,35] treatment was used to determine whether this could explain the TEM observations. The LSW model predicts the following size distribution for particles of radius r:

$$g(r/\bar{r}) = g(z) = \begin{cases} \frac{3^4}{2^{5/3}} \frac{z^2 \exp\left(\frac{2/3\,z}{2/3\,z-1}\right)}{(z+3)^{7/3}(3/2-z)^{11/3}} & \text{if} \quad 0 < z < 3/2 \\ 0 & \text{else} \end{cases} \tag{1}$$

where $z = r/\bar{r}$ and $\bar{r}$ is the average radius. Average quantities, $\langle x \rangle$, are calculated from the distribution in the usual way:

$$\langle x(t) \rangle = \frac{\int dr\; g(r,t) x(r,t)}{\int dr\; g(r,t)} \tag{2}$$

Because $\bar{r}$ increases with time, the singly peaked distribution shifts and broadens with time, as is illustrated in Fig. 2. Assuming a lower limit for crystal detection of 2.5 nm radius (following the earlier discussion), if the initial distribution lies completely below this size, no crystallites are observed. As the distribution evolves beyond the detection limit, new particles appear, mimicking nucleation and growth and hiding the actual coarsening character of the transformation.

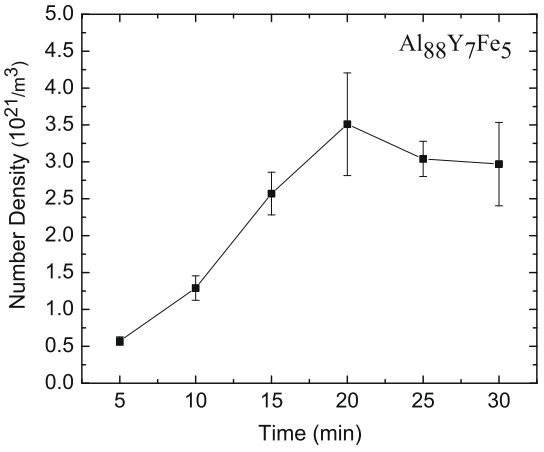

Fig. 1. Number density of α-Al crystallites during annealing at 250 °C from bright field TEM images. The increase in number density with increased annealing time is characteristic of a nucleation and growth dominated transformation.

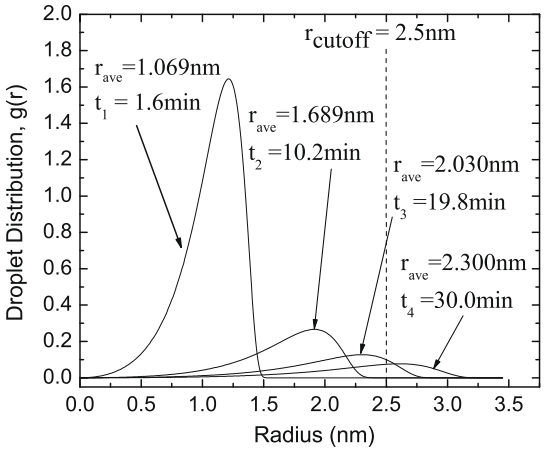

Fig. 2. Evolution of a sample droplet distribution given by LSW coarsening theory. As the droplet distribution evolves in time, the average radius increases and the distribution spreads. For this example (TEM visualization cutoff of 2.5 nm) the distribution initially lies completely below the cutoff and the true character of the transformation is hidden.

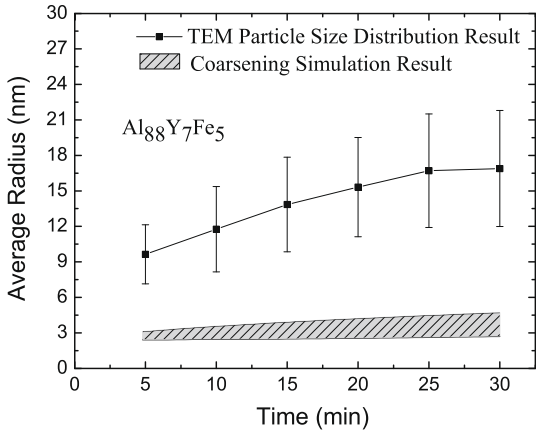

Fig. 3. Comparison between the TEM particle-size distribution result for average radius and the coarsening model when corrected for the TEM visualization cutoff. The coarsening model data is presented as the range of all possible values bounded on the low side by the value of the initial radius that gives observable crystallites at 5 min of annealing and the high side by the lack of observable crystallites in bright field TEM images of as-quenched samples.

This was investigated further by calculating the average radius as a function of annealing time at 250 °C for coarsening, and comparing it with the data obtained from the TEM investigations. The growth of the average radius was assumed to follow the result from LSW theory for diffusion-limited growth

$$\bar{r} = (r_0^3 + k(T)t)^{1/3} \tag{3}$$

where r_0 is the initial average radius and $k(T)$ is the isotropic volume growth rate per unit time. Following Chen and Spaepen [31], the evolution of the interfacial enthalpy can be written as

$$-\dot{H} = \left(\frac{H_0 r_0}{3}\right) \frac{k(T)}{\left[r_0^3 + \frac{k_B T^2 k(T)}{Qb}\right]^{4/3}} \tag{4}$$

where $\dot{H}$ is the time rate of enthalpy release (measured as a function of temperature in DSC non-isothermal scans), H_0 is the total enthalpy of transformation, k_B is Boltzmann's constant, Q is the apparent activation energy of the transformation, and b is the scan rate. All quantities (except the initial radius) were extracted from non-isothermal DSC experiments at 5 scan rates: 10 °C min^{-1}, 20 °C min^{-1}, 40 °C min^{-1}, 60 °C min^{-1}, and 80 °C min^{-1}. The Curie transition of Ni, which was not a function of scan rate, was measured simultaneously to correct for the contribution of instrumental transients to the shifts in the peak of the transition with scan rate. Based on a Kissinger analysis [39] of the corrected data, the effective activation energy for the transformation is 2.62 ± 0.03 eV. By integrating the enthalpy released over time, $H_0 = 19.07 \pm 0.43$ J g^{-1}.

Eq. (4) was solved to obtain $k(T)$ for a range of initial radii, r_0, since it could not be determined from calorimetric data. The average radius, $\bar{r}$, was computed as a function of annealing time at 250 °C using these values for $k(T)$ and the lower bound stated earlier for the radius of crystal that could be observed (2.5 nm). The error in the experimentally determined average radius was calculated from the standard deviation. The calculated and measured values of $\bar{r}$ are shown in Fig. 3.

Predictions from the coarsening model are in poor agreement with the experimental data. Taken in concert with electrical resistivity and APT results discussed later in this section, it is clear that the anomalous DSC isothermal data signal corresponds to a nucleation and growth process and not coarsening. From Fig. 1 the nucleation rate is very high, approximately 3×10^{18} m^{-3} s^{-1}; growth is likely very slow, dominated by the diffusion rate of Y in the glass [14].

3.2. Electrical resistivity measurements

Measurements of the change in electrical resistivity using a four-probe technique allow quantitative studies of the phase transformation kinetics over a wider temperature range than are possible with DSC or other calorimetric techniques [23]. The nucleation rates for α-Al in $Al_{88}Y_7Fe_5$ glasses are so high and the crystal growth rates are so slow that the earliest stages of the transformation are likely buried in the instrumental transients of DSC and later enthalpy releases are very small [32]. Taken with the coarsening studies just discussed, the featureless DSC isothermal curves, such as those obtained for the primary crystallization of $Al_{88}Y_7Fe_5$, do not reflect the true nature of the transformation.

The electrical resistance of the partially devitrified nanocomposite, consisting of the α-Al phase (volume fraction f_α and resistivity ρ_α) embedded in an amorphous phase (volume fraction f_m and resistivity ρ_m) is [40].

$$\rho_{\text{sample}} = \frac{\rho_m}{2}(1 - f_\alpha/x) + \frac{\rho_\alpha}{2}(1 - f_m) + \left(\left[\frac{\rho_m}{2}(1 - f_\alpha/x) + \frac{\rho_\alpha}{2}(1 - f_m)\right]^2 - \rho_m \rho_\alpha (1 - 1/x)\right)^{1/2} \tag{5}$$

The crystal phase is modeled as an ellipsoid of revolution with eccentricity x. Because the resistivity of the $Al_{88}Y_7Fe_5$ is much greater than that of the α-Al ($\sim 2 \times 10^{-6}\,\Omega\,m$ compared with $2.6 \times 10^{-8}\,\Omega\,m$ at room temperature), changes in the measured resistivity will be dominated by the growth of the α-Al phase. The measured resistivity of the sample (ρ_{sample}) is then approximately

$$\rho_{sample} \approx \rho_m(1 - f_\alpha/x) \quad (6)$$

This approximation has been experimentally validated. The rate of enthalpy released, dH/dt scales linearly with the rate of volume fraction transformed. From Eq. (6), the magnitude of $d\rho_{sample}/dt$ should scale in the same way. Measured values for $|d\rho_{sample}/dt|$ and $|dH/dt|$ for a non-isothermal scan (Fig. 4) of the as-quenched samples at 2 °C min^{-1} from room temperature to 400 °C showed the same peak shape, with an onset at 255 °C and a maximum at 265 °C. The similarities of the two sets of data in Fig. 4 confirm the approximations made in Eqs. (5) and (6), allowing these equations to be used to quantitatively analyze the crystallization kinetics in isothermal studies.

The changes in resistance of rapidly quenched samples $Al_{88}Y_7Fe_5$ with isothermal annealing were measured as a function of time for several annealing temperatures that were below the onset of significant α-Al crystallization measured in a non-isothermal scan. The sample temperature measured during isothermal annealing was stable to ±0.5 °C over 80 h. The data were generally collected until the resistance change appeared to be near saturation; within their limit of sensitivity, XRD measurements confirmed that the transformation product was only α-Al.

The measured normalized resistivity values (resistance normalized to the initial resistance, assuming no changes in sample volume) for isothermal anneals at 215 °C, 235 °C, 240 °C, 245 °C, and 250 °C are shown in Fig. 5. Although the data for the higher annealing temperatures show a monotonic decrease in resistivity, consistent with

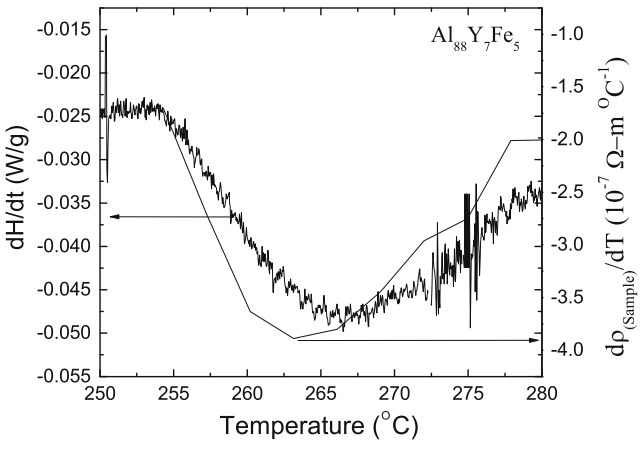

Fig. 4. Comparison between measured values for $|d\rho_{sample}/dt|$ and $|dH/dt|$ for a non-isothermal scan of the as-quenched samples at 2 °C min^{-1} from room temperature to 400 °C. The similarity of the peak shape and position validate the assumption that the resistance is proportional to the volume fraction transformed of crystalline α-Al.

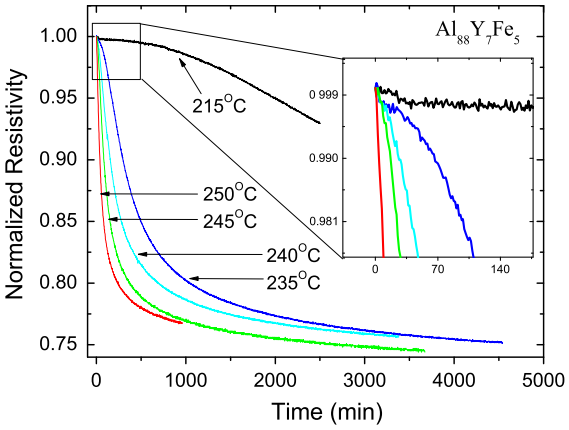

Fig. 5. Normalized resistivity changes during isothermal annealing at various temperatures of as-quenched $Al_{88}Y_7Fe_5$.

the DSC data and reminiscent of coarsening, the lower temperature data (215 °C and 235 °C) show the expected sigmoidal-type behavior (i.e., change from an initially negative to positive curvature in the plot of resistance as a function of time). This behavior is consistent with a nucleation and growth transformation. For clarity, the resistivity change with annealing at 215 °C for short times is included to clearly show the plateau in the initial stage of the transformation (inset in Fig. 5, from 35 min $< t <$ 200 min). All resistance data show a small (~0.25%) resistance decrease due to probe settling near the beginning of the run, accounting for the decrease in resistance observed near 35 min for the 215 °C isothermal anneal (inset). To allow the initial plateau of the sigmoidal curve to be observed in contrast with the data from the higher temperature, the 215 °C data set was truncated. The curvature inflection of the sigmoidal curve occurs near an annealing time of 5000 min for that data. The rate of change of the electrical resistivity decreases for long annealing times in all data sets. This long-time behavior was fit well to an exponential function; all data converged to the same long-time asymptotic normalized resistance of 0.748 ± 0.008. Like the isothermal DSC results, the lack of a sigmoidal character at high temperatures can be explained by a high nucleation rate, causing the rapid production of a high density of nanocrystals [32]. This rapid transformation occurs during the instrumental transient and is not observed. The observed change in resistance at those temperatures reflects further growth and coarsening of the nanocrystals.

3.3. Evidence for phase separation prior to crystallization

From the APT studies, atom maps were constructed for the as-quenched $Al_{88}Y_7Fe_5$ alloy. A high density (10^{24}–10^{25} m^{-3}) of pure Al zones (henceforth referred to as "pure Al nanoregions") is observed, some containing up to 50 atoms, when corrected for the detection efficiency of the LEAP. This is demonstrated in Fig. 6, showing the calculated probability of having no solute atoms in regions of

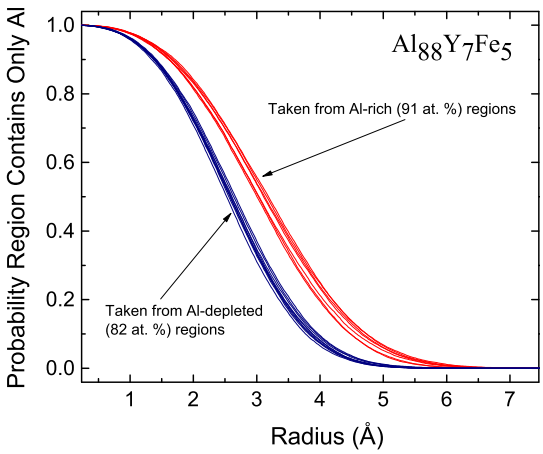

Fig. 6. The probability, in percent, that a region of a given size will contain no solute atoms, computed from the APT data for $Al_{88}Y_7Fe_5$. The different curves correspond to different cubes of data. The set of red curves correspond to cubes located in the Al-rich (91 at.%) regions of the sample, while the set of blue curves correspond to cubes located in Al-depleted regions (82 at.%). (For interpretation of the references to color in this figure legend, the reader is referred to the web version of this article.)

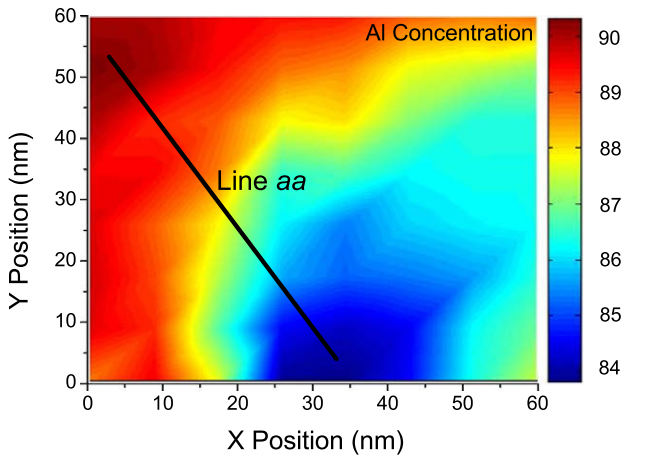

Fig. 7a. Al concentration profile in the $Al_{88}Y_7Fe_5$ glass. An interpolating polynomial has been used for shading the areas other than the cube centers, for which the data is available. The color bar on the side shows the color coding for the concentration (in at.%).

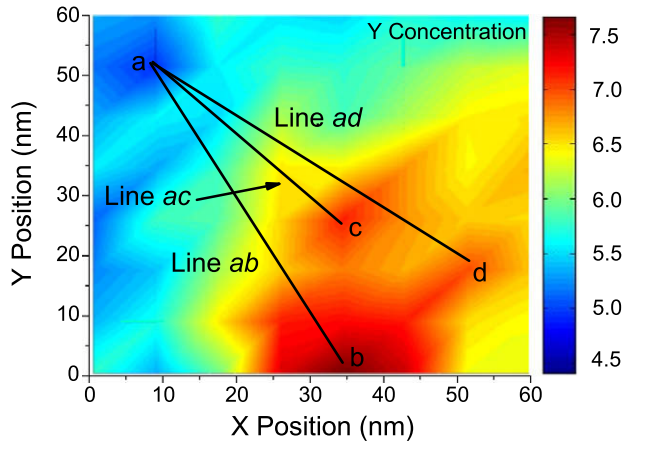

Fig. 7b. Y concentration profile in the $Al_{88}Y_7Fe_5$ glass. The lowest Y concentration is 5.0% while the highest is 7.9%. The cuts *ab*, *ac* and *ad* are approximately 59, 37 and 56 nm, respectively.

different radius. The data set is discretized, and each curve in Fig. 6 shows the probability distribution within each discrete region. The results fall into two different groups, suggesting a fluctuation over a length scale that is larger than the region size. No evidence of crystallographic planes was observed in these pure Al zones. Such a high density of pure Al zones has not been experimentally observed previously, although it is consistent with a statistical random distribution of the solvent atoms [41]. In a later publication, we will demonstrate that a quantitative analysis of these data show that the distribution of pure Al zones is random spatially, in agreement with earlier predictions [45].

To investigate possible chemical inhomogeneity on a length scale longer than the nanometer sized pure Al regions, the chemical composition is averaged over cubes of edge length 8.75 nm. A longer-range chemical fluctuation is confirmed in Fig. 7a, showing a separation between Al-rich (91 at.%) and Al-depleted (82 at.%) along line *aa*. As expected, these are anti-correlated with the solute-rich regions (Figs. 7b and 7c). An interpolating polynomial shading scheme was used to produce a continuous compositional map. We will show later in this section that this does not introduce artifacts into the results. By direct spatial comparison, the measured chemical fluctuations are found not to be correlated with the species-independent atom collection density (Fig. 7d), indicating that they are real and not a function of the any biased counting efficiency.

In APT, the atomic species is determined from time of flight mass spectrometry. Since there is a Fe^{++}/Al^{+} overlap of the mass-to-charge state, Y data were used to determine the nature of the spatial fluctuation. The Y concentration along the line *ac* in Fig. 7b is shown in Fig. 8. As expected from Figs. 7a–d, the fluctuation is not random, but suggests chemical phase separation. No interpolation was used for these data. That they agree with the trends observed in Figs. 7a–d indicates that the interpolation scheme used to produce the concentration maps introduces no measurable artifacts. Line *aa* in Fig. 7a is approximately 63 nm in length; lines *ab*, *ac* and *ad* in Fig. 7b are approximately 59, 37 (plotted in Fig. 8) and 56 nm in length, respectively. Unfortunately, the volume of analysis was too small to obtain APT data over a sufficiently large region to observe a complete wavelength. Assuming, however, that the fluctuations roughly follow a sinusoidal pattern, these distances correspond to a half wavelength (minimum to maximum), indicating a length scale for phase separation of 74 to 126 m.

Competition between diffusion and interfacial attachment can dramatically decrease the nucleation rate [42]. Therefore, the data suggest that the formation of α-Al during annealing occurs in the pure Al nanoregions located in the high aluminum concentration regions of the sample.

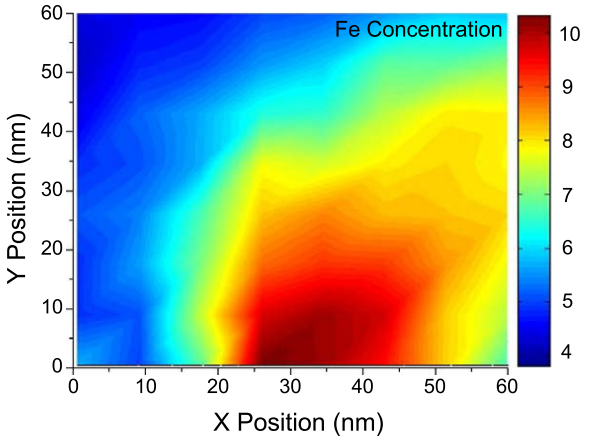

Fig. 7c. Fe concentration profile in the $Al_{88}Y_7Fe_5$ glass. The highest and lowest Fe concentrations are 10.3% and 4.2% respectively.

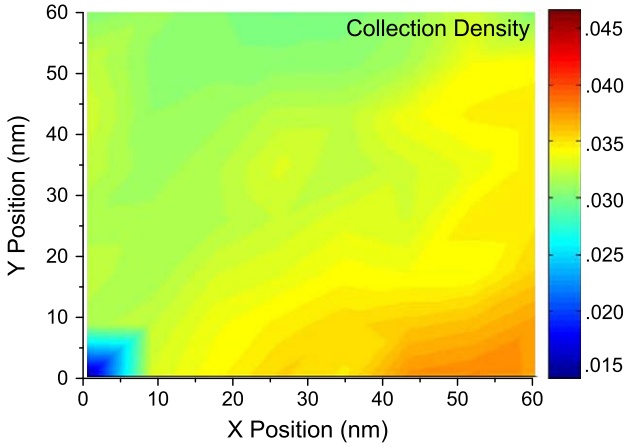

Fig. 7d. The collection density the $Al_{88}Y_7Fe_5$ glass. The lack of correlation of the fluctuations in (d) with those in (a–c) indicates the concentration fluctuations are not artifacts of preferential loss of particular atom species.

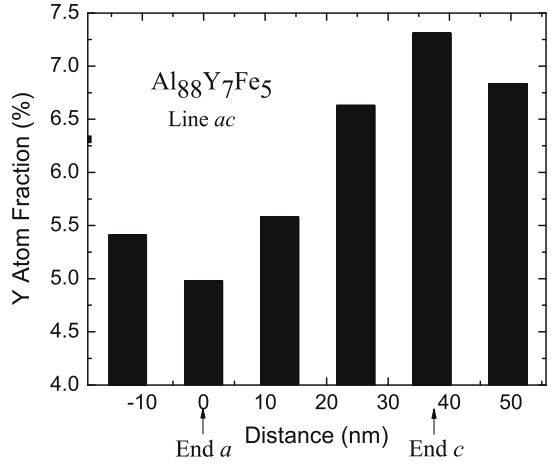

Fig. 8. The Y concentration profile along line *ac* of Fig. 7b showing a smooth profile between a local minimum and a local maximum. Two extra cubes have been added to clarify the sinusoidal profile. This profile partly validates the interpolating polynomial shading scheme used in Fig. 7 and indicates that there is no sharp interface between the phase separated regions.

Guidance can be obtained by using the classical theory of nucleation [17] to estimate the critical size and nucleation rate. Calculating the driving free energy from the measured enthalpy, assuming the measured interfacial free energy for α-Al and its melt [17], and using the measured crystal growth rate [14,15] to estimate the interfacial mobility, the critical size for nucleation of α-Al from a pure Al liquid (or glass) at these temperatures is approximately 120 atoms and the nucleation rate is approximately $10^{21}\,m^{-3}\,s^{-1}$. Note that this is an underestimate of the rate, since the measured growth rate used was likely dominated by Y diffusion [14,15]. Most of the pure Al nanoregions are much smaller than the critical size (Fig. 6), however, causing the actual nucleation rate to be less than would be expected. Assuming the estimated rate, only 1 in 1000 to 1 in 10,000 of the pure Al nanoregions (total number of order 10^{24}–$10^{25}\,m^{-3}$) would need to nucleate α-Al to account for the crystallite number density observed (Fig. 1). Based on the observed length scales of phase separation (74–126 nm) the density of Al-rich regions is between $5 \times 10^{20}\,m^{-3}$ and $3 \times 10^{21}\,m^{-3}$, the same order as the number of α-Al crystallites in the fully nucleated sample, suggesting that on average only one of the pure Al nanoregions in each Al-rich region forms an α-Al that grows. Once nucleated and grown to a size larger than the pure Al nanoregion, the α-Al grows by diffusion-limited rejection of Y [14,15]. Soft impingement of the crystallites quickly shuts down further nucleation and growth, resulting in the amorphous/nanostructured material observed. While the nucleation estimates are made by extrapolating the classical theory into a regime of metastability where it is likely not quantitatively valid, the predicted trends remain qualitatively correct.

Given the extremely high nucleation rate one might argue that the pure Al nanoregions would already be transformed in the as quenched sample. However, high HRTEM studies showed no evidence for this. The HRTEM images were featureless, as expected for a metallic glass, with no observed regions containing lattice fringes. Rastered nanoprobe diffraction studies (using a probe diameter of 1.2 nm) also gave no evidence for nanocrystallization [43]. However, they did reveal medium-range order in the glass, with a coherence length of 1.7 nm and a local order like that expected for crystal Al. Similar observations were reported earlier for Al–Sm [9]. These ordered regions are likely the pure Al nanoregions observed in the APT measurements. Even though they are not "crystals" in the conventional sense, the existing order would substantially lower the nucleation barrier for the α-Al, making them a type of "quenched-in nuclei" as has been suggested previously [8,14].

4. Conclusions

In conclusion, quantitative studies of the crystallization of rapidly quenched $Al_{88}Y_7Fe_5$ alloys show that the transformation initially proceeds by rapid nucleation and not by coarsening as was proposed earlier [44]. Previous

studies [14] suggest that given the composition difference between the crystallization product (face-centered cubic Al) and the nominal composition of the matrix, the initial nucleation step is followed by slow diffusion-controlled growth. Based on APT measurements, we present the first evidence for nanoscale phase separation into Al-rich and Al-poor regions in these alloys. The pure Al zones in Al-rich regions likely are the sites for the rapid nucleation of α-Al, where the nucleation barrier is small. The tendency for many Al-based metallic glasses to crystallize to a amorphous/nanocrystal composite and the recently reported evidence for phase separation in a related glasses ($Al_{89}Ni_6La_5$) [19] raises the question of whether nanoscale phase separation is common in Al-based glasses.

Acknowledgements

The research was partially supported by the National Science Foundation under Grants DMR-06-06065, DMR-08-56199, and the US Air Force Office of Scientific Research under Contract FA9550-05-1-0110. The APT research at the Oak Ridge National Laboratory SHaRE User Facility was sponsored by the Scientific User Facilities Division, Office of Basic Energy Sciences, US Department of Energy. The synchrotron measurements were made on the MUCAT beam-line at the Advanced Photon Source. Work in the MUCAT Sector at the APS, and the Ames Laboratory was supported by the Department of Energy, Basic Energy Sciences, under Contract No. DS-AC02-07CH11358. Use of the Advanced Photon Source was supported by the US Department of Energy, Office of Science, Office of Basic Energy Sciences, under Contract No. DE-AC02-06CH11357.

References

[1] Peker A, Johnson WL. Appl Phys Lett 1993;63:2342.
[2] Lin XH, Johnson WL. J Appl Phys 1995;78:6516.
[3] Inoue A, Nakamura T, Nishiyama N, Masumoto T. Mater Trans JIM (Jpn Inst Met) 1992;33:937.
[4] Bondi KS, Gangopadhyay AK, Marine Z, Kim TH, Mukhopadhyay A, Goldman AI, et al. J Non-Cryst Solids 2007;353:4723.
[5] Hong SJ, Warren PJ, Chun BS. Mater Sci Eng A 2001;31.
[6] Perepezko JH, Hamann J, Hebert RJ, Rosner H, Wilde G. Mater Sci Eng A 2007;449:84.
[7] Calin M, Köster U. Mater Sci Forum 1997;269:749.
[8] Perepezko JH, Hebert RJ, Wu RI, Wilde G. J Non-Cryst Solids 2003;317:52.
[9] Stratton WG, Hamman J, Perepezko JH, Voyles PM, Mao X, Khare SV. Appl Phys Lett 2005;86:141910.
[10] Inoue A, Ohtera K, Tsai A-P, Masumoto T. Jpn J Appl Phys 1988;27:L280.
[11] Zhang Y, Warren P, Cerezo A. Mater Sci Eng A 2002;327:109.
[12] Omata S, Tanaka Y, Ishida T, Sato A, Inoue A. Philos Mag A 1997;76:1477.
[13] Tsai AP, Kamiyama T, Kawamura Y, Inoue A, Masumoto T. Acta Mater 1997;45:1477.
[14] Foley JC, Allen DR, Perepezko JH. Scripta Mater 1996;35:655.
[15] Allen DR, Foley JC, Perepezko JH. Acta Metall 1997;46:431.
[16] Gloriant T, Ping DH, Hono K, Greer AL, Baro MD. Mater Sci Eng A 2001;304–306:315.
[17] Kelton KF. In: Ehrenreich H, Turnbull D, editors. Solid state physics. Boston: Academic Press; 1991.
[18] Kelton KF, Greer AL. J Non-Cryst Solids 1986;79:295.
[19] Radiguet B, Blavette D, Wanderka N, Banhart J, Sahoo KL. Appl Phys Lett 2008;92:103126.
[20] Tanner LE, Ray R. Scr Metall 1980;14:657.
[21] Park BJ, Chang HJ, Kim DH, Kim WT, Chattopadhyay K, Abinandanan TA, et al. Phys Rev Lett 2006;96:245503.
[22] Wang WC, Li JH, Zeng F, Gu YL, Liu BX. J Alloy Compd 2009;478.
[23] Gangopadhyay AK, Croat TK, Kelton KF. Acta Mater 2000;48:4035.
[24] Nagahama D, Ohkuba T, Hono K. Scripta Mater 2003;49:729.
[25] Na JH, Kim YC, Kim WT, Kim DH. Met Mater Int 2008;14:553.
[26] Tian N, Ohnuma M, Ohkubo T, Hono K. Mater Trans 2005;46:2880.
[27] Kelton KF, Holzer JC. Rev Sci Instrum 1988;59:347.
[28] Kelly TF, Miller MK. Rev Sci Instrum 2007;78:031101.
[29] Miller MK. Atom probe tomography. New York, NY: Springer; 2000.
[30] Herbert RJ, Boucharat N, Perepezko JH, Rosner H, Wilde G. J Alloy Compd 2007;434:18.
[31] Chen LC, Spaepen F. J Appl Phys 1991;69:679.
[32] Kelton KF. J Alloy Compd 2006;434–435.
[33] Bassim N, Kiminami CS, Kaufman MJ. J Non-Cryst Solids 2000;273.
[34] Lifshitz IM, Slyozov VV. J Phys Chem Solids 1961;19:35.
[35] Wagner KC. Z Electrochem 1961;65:581.
[36] Saltykov SA. Stereometric metallography. Moscow: Metallurgizdat; 1958.
[37] Xu Y-H, Pitot HC. Comput Methods Programs Biomed 2003;72:1.
[38] Landau LD, Lifshitz EM. Statistical physics, part 1. 3rd ed. Elsevier; 1980.
[39] Kissinger HE. Anal Chem 1957;29:1702.
[40] Davidson A, Tinkham M. Phys Rev B 1976;13:3261.
[41] Spowart JE, Miracle DB, Mullens HM. J Non-Cryst Solids 2004;336.
[42] Kelton KF. Acta Mater 2000;48:1967.
[43] Daulton TL, Bondi KS, Kelton KF. Ultramicroscopy. Submitted for publication.
[44] Xing LQ, Mukhopadhyay A, Buhro WE, Kelton KF. Philos Mag Lett 2004;84:293.
[45] Sahu KK, Nussinov Z. Private communication, 2009.